Journal Pre-proofs

Bayesian analysis of critical fatigue failure sources

Joona Vaara, Miikka Väntänen, Panu Kämäräinen, Jukka Kemppainen, Tero Frondelius

PII: S0142-1123(19)30386-X
DOI: https://doi.org/10.1016/j.ijfatigue.2019.105282
Reference: JIJF 105282

To appear in: *International Journal of Fatigue*

Received Date: 5 March 2019
Revised Date: 13 September 2019
Accepted Date: 16 September 2019

Please cite this article as: Vaara, J., Väntänen, M., Kämäräinen, P., Kemppainen, J., Frondelius, T., Bayesian analysis of critical fatigue failure sources, *International Journal of Fatigue* (2019), doi: https://doi.org/10.1016/j.ijfatigue.2019.105282

Bayesian analysis of critical fatigue failure sources

Joona Vaara[a,*], Miikka Väntänen[b], Panu Kämäräinen[a], Jukka Kemppainen[c], Tero Frondelius[a,d]

[a] *Wärtsilä, Järvikatu 2-4, 65100 Vaasa, Finland*
[b] *Global Boiler Works Oy, Lumijoentie 8, 90400 Oulu, Finland*
[c] *Applied and Computational Mathematics, Pentti Kaiteran katu 1, 90014 University of Oulu, Finland*
[d] *Materials and Mechanical Engineering, Pentti Kaiteran katu 1, 90014 University of Oulu, Finland*

Abstract

A novel approach for inferring the underlying non-metallic inclusion distribution from fatigue test fractography is presented. It is shown that the non-metallic inclusion size distribution obtained from fatigue testing differs from the extreme value distributions, which do not take fatigue into account. Fatigue, as a process, acts as a filter for the observed inclusions, and by taking advantage of this allows us to extract more refined information from the fractography using statistical inference. The emphasis in this paper is on analysis of axial fatigue testing of smooth specimens. The concepts presented here apply to all fatigue testing where the data from fracture surfaces is collected.

Keywords: Bayesian inference, Extreme values, Fatigue size effect, Fractography, Inclusion size distribution

1. Introduction

Manufacturing large volume castings and components of high quality is not an easy task. With increased volume, the fatigue properties tend to decrease – a phenomenon known as the fatigue size effect. Weibull's weakest-link (WL) theory [1] has been employed to explain the effect with statistically distributed defects or flaws in the material [2]. The larger the volume, the

*Corresponding author
Email address: joona.vaara@wartsila.com (Joona Vaara)

larger the expected flaw size. The typical formulation assumes the critical defect size and applied stress to follow a power-law relationship and the largest defect to follow a Fréchet extreme value distribution [3]. With these assumptions the defect size becomes an auxiliary variable, as the survival probability is expressed using effective stresses, highly stressed volume, Weibull-exponent and the fatigue limit. The developments of this statistical framework focus on finding the correct multiaxial fatigue criterion complying with the observations [4, 5], the selection of the defect size distribution and the methods fitting these distributions [6, 7, 8, 9, 10, 11, 12, 13].

The weakest-link theory based methods have recently received criticism for their inability to predicting notched fatigue test results [5]. On the other hand, the method has seen quite some success in predicting various loading and specimen geometries [4, 2]. The prediction errors of volume based WL-method shown in [3] were improved from local stress concepts. The well-known benchmark data set for the fatigue size effect is the fatigue test series for 30CrNiMo8 by Böhm [14] and Magin [15] containing a combination of 26 different specimen geometries or loading conditions. The WL-concept has been extended for combined surface and internal failures and various loading cases [16, 4]. Specimen geometry with two distinct competing notches as possible failure initiation locations was developed and studied in [17, 18, 5]. The WL-based model was reported to fail in capturing the experimental outcome of two competing notches. Recently, the WL-concept was successfully applied to predict fatigue behavior with varying number and diameter of artificial surface defects for 7050 aluminium alloy [19]. The same group then applied the model to predict the fatigue strength of various surface roughness levels obtained by milling [20]. In both cases, the predictions from volume based model were reported to better agree with the experimental results. A layer with depth of 50 µm from the surface was considered, unlike in the original WL-volume formulation. This was justified with the observation of intermetallic particles in the vicinity of the crack initiation site for large portion of the specimens. A similar concept was proposed in [5] to enhance the prediction capability. The physical problem is inevitably two-fold: first, there exist statistically distributed non-metallic inclusions/defects and second, how the inclusions affect the fatigue properties. What is observed from fracture surfaces of fatigue testing is the outcome of both problems.

The surface effects from stereology [21] were incorporated analytically by Cetin *et al.* in [22] to model the statistically distributed defects with a strong physical basis. The log-normal based total failure probability predictions matched well for several specimen geometries in Böhm's axial fatigue test-set but failed for some of the specimens with minimal notch radius. Non-propagating cracks [23] controlling the fatigue of these specimen was proposed as a possible explanation. Their work acts as a solid foundation for the development of statistical likelihood-based methods predicting the non-metallic inclusion distribution.

The tests performed in [24, 13] show significantly smaller nitrides being found from fracture surfaces than the oxides. Recent studies have reported different fatigue properties for different inclusion compositions [25, 26, 27]. Mixture model and competing risks approaches have been developed for analyzing materials containing multiple defect types [28]. Cetin *et al.* [13] categorized inclusions by composition and made predictions from each distribution separately. In their paper, they successfully applied log-normal distribution to fit the polished cross-section data and to predict the fracture surface observations of smooth axial fatigue tests for 100Cr6. The statistics of extremes have been successfully applied to analysis of non-metallic inclusions in various materials, graphite spheroids in ductile cast irons, pores in cast aluminium, hard second phases (in Al-Si eutectic alloys) and carbides in tool steels [29].

Our analysis is built on the statistical methodology presented in [22] for fracture surface observations from axial smooth fatigue specimens by using the Generalized Pareto Distribution. The objective of the current study is to extend the statistical analysis to more thoroughly include the fracture surface observations. Different fatigue failure sources, including locations (surface or internal), are distinguished in the analysis. The corresponding analytical likelihood is built with analysis of competing failure modes. The observation at fracture surface is the critical fatigue failure source in the specimen.

2. Model

2.1. Non-metallic inclusion size distribution

We assume that the sizes of potentially dangerous non-metallic inclusions can be described by Generalized Pareto Distribution (GPD). The application of GPD to analysis of non-metallic inclusion extreme values has been studied extensively by one research group [12, 30, 31, 7, 32, 33]. GPD is a peak over threshold (PoT) method, where every occurrence exceeding predetermined threshold is counted instead of counting only block (inspection volume) maxima (BM). Three extreme value distribution families (I, II and

III) exist, determined by the shape parameter ξ and characterized by the distribution tail behavior. The parameters of GPD are uniquely determined by those of the associated BM Generalized Extreme Value (GEV) distribution [34]. Saturation of the fatigue size effect was reported to occur for ductile cast iron at highly stressed volume 8000 mm^3 [35], whereas a continuous decrease of fatigue limit has been reported for 30CrNiMo8 even with highly stressed volumes up to 100000 mm^3 [36] – indicating that the model needs to be flexible enough to describe both kinds of saturation behavior.

2.1.1. Base size distribution

The analytical formulation shown below was first derived by Cetin *et al.* for log-normally distributed inclusion size in [22]. We follow their example here and derive the model for GPD. We say that a random variable X follows a GPD distribution and write $X \sim \mathrm{GPD}(\mu, \sigma, \xi)$, if the probability density function of X is

$$f(x \mid \mu, \sigma, \xi) = \frac{1}{\sigma}\left(1 + \xi\frac{(x-\mu)}{\sigma}\right)^{-\frac{1}{\xi}-1}, \tag{1}$$

where $\mu \in \mathbb{R}$ is the location parameter, $\sigma > 0$ is the scale parameter and $\xi \in \mathbb{R}$ is the shape parameter. We choose the shape parameter as $\xi < 0$, which corresponds to the Type III extreme value distribution yielding an upper limit to the size of the non-metallic inclusions that is more in line with the expectation from steelmaking practice [7, 31]. Then X is supported on the finite interval $[\mu, \mu - \sigma/\xi]$ and the cumulative distribution function is

$$F(x \mid \mu, \sigma, \xi) = 1 - \left(1 + \xi\frac{(x-\mu)}{\sigma}\right)^{-\frac{1}{\xi}}, \quad \mu \le x \le \mu - \sigma/\xi. \tag{2}$$

At this point it is necessary to make the choice what is the variable that follows GPD. The GPD distribution has a nice scaling property. Namely, if we choose that the base parametrization is for the diameter D of the inclusion, that is $D \sim \mathrm{GPD}(\mu, \sigma, \xi)$, then $\sqrt{\text{area}} := \sqrt{\frac{\pi}{4}}D$ follows the $\mathrm{GPD}(\hat{\mu}, \hat{\sigma}, \xi)$ distribution with the modified location and scale parameters $\hat{\mu} := \sqrt{\frac{\pi}{4}}\mu$ and $\hat{\sigma} := \sqrt{\frac{\pi}{4}}\sigma$. The upper limit for inclusion size in $\sqrt{\text{area}}$ is then

$$x_{\max} := \hat{\mu} - \frac{\hat{\sigma}}{\xi}, \quad \xi < 0. \tag{3}$$

2.1.2. Internal size distribution

Assuming the number of inclusions exceeding the threshold size μ to follow Poisson distribution, with inclusion density ρ the expected number of inclusions found in volume is ρV, leads to the cumulative distribution function

$$F_{\text{int}}(x \mid \mu, \sigma, \xi) = \exp\left[-\rho V_{\text{int}}\left(1 - F(x \mid \hat{\mu}, \hat{\sigma}, \xi)\right)\right] \tag{4}$$

for the largest inclusion in the volume denoted by $\sqrt{\text{area}}_{\text{max-int}}$. We added subscript *int* for internal. The density function is obtained by differentiating (4) with respect to x:

$$f_{\text{int}}(x \mid \mu, \sigma, \xi) = \rho V_{\text{int}} f(x \mid \hat{\mu}, \hat{\sigma}, \xi) F_{\text{int}}(x \mid \mu, \sigma, \xi). \tag{5}$$

2.1.3. Surface size distribution

For surface distribution there are three additional things that need to be accounted for [22]:

- The larger sizes are more likely to penetrate the surface, producing a size-weighted distribution towards the larger [21]
- The effective surface volume, or number of inclusions penetrating the surface [21]
- Cutting of the free surface (machining) modifying the effective size distribution

A well-known result in stereology is that the effective surface volume is

$$V_{\text{surf}} = A_{\text{surf}} \frac{\mathbb{E}(D)}{1000}, \tag{6}$$

where A_{surf} is the surface area in mm^2, $\mathbb{E}(D) = \mu + \frac{\sigma}{1-\xi}$ is the expected diameter of inclusions in µm. We assume here area, volume and inclusion density to be expressed in millimeters whereas the rest of the parameters are in micrometers. The inner volume is then

$$V_{\text{int}} = V_{\text{tot}} - V_{\text{surf}}, \tag{7}$$

where V_{tot} is the homogeneously stressed total volume. The size-weighted distribution for diameter of inclusions penetrating the surface is [21]

$$F_{D_{\text{surf}}}(d \mid \mu, \sigma, \xi) = \frac{1}{\mathbb{E}(D)} \int_0^d t dF(t \mid \mu, \sigma, \xi). \tag{8}$$

Cetin *et al.* [22] show an efficient way of modeling the cutting of inclusions with the function $h(u)$

$$\sqrt{\text{area}}(u) = d\sqrt{\frac{\pi}{4} - \frac{\arccos u}{4} + \frac{\sin(2\arccos u)}{8}} = h(u)d, \tag{9}$$

where $u = \frac{r}{R}$ is the distance from the cut to the center of the inclusion r normalized by the radius of the inclusion R. r is negative when the center of the inclusion is outside of the material. This can be assumed to be a random variable following uniform distribution $u \sim \mathcal{U}(-1, 1)$. It follows then that the distribution function for the maximum surface defect size $\sqrt{\text{area}}_{\text{max-surf}}$ is

$$F_{\text{surf}}(x \mid \mu, \sigma, \xi) = \exp\left[-\frac{\rho V_{\text{surf}}}{2}\int_{-1}^{1}\left(1 + \frac{x - h(u)\mu}{(1-\xi)h(u)\mathbb{E}(D)}\right)(1 - F(x \mid h(u)\mu, h(u)\sigma, \xi))\,du\right]. \tag{10}$$

The density function is obtained again by differentiating (10) with respect to x:

$$f_{\text{surf}}(x \mid \mu, \sigma, \xi) = \frac{\rho V_{\text{surf}}}{2}\int_{-1}^{1}\left[\frac{x}{h(u)\mathbb{E}(D)} f(x \mid h(u)\mu, h(u)\sigma, \xi)\right] du F_{\text{surf}}(x \mid \mu, \sigma, \xi). \tag{11}$$

The formulation is now complete. Being able to write these analytical expressions allows the use of likelihood-based fitting methods.

2.1.4. Other choice for size distributions

Murakami and co-workers have employed Type I GEV distribution for their analysis method often labeled as Statistics of Extreme Values (SEV) [6, 37, 11]. In [29] they agree that an upper limit for the defect size should exist, but the type I extreme value distribution has been sufficient to describe the inclusion sizes obtained from fatigue tests with various volumes (20 - 1000 mm^3). Critique has been raised regarding the sensitivity of the large volume extrapolation values with respect to the slope parameter, the method not considering all the available data due to the BM nature, the lack of saturation (upper limit for inclusion size) as prediction volume increases and potentially over-optimistic estimates of prediction accuracy [7, 32].

Log-normal distribution has been employed by several authors [8, 22, 10, 13]. The distribution will asymptotically approach the Type I extreme value distribution as the prediction volume tends to infinity. Type II GEV distribution is the most commonly used with the WL-method [2, 4, 16, 3].

The type III GPD distribution has an upper limit for the inclusion size, and differing from type III GEV distribution, also a lower limit. It allows the use of more data when fit to optical microscopy samples, not only the block maximum. These characteristics are desirable for the distribution suitable for our purposes.

2.2. Parameters

Bayesian inference was employed in this paper to obtain stochastic estimates of the model parameters. The use of Bayesian inference in fatigue data analysis and design of experiments has recently been studied in [38, 39]. The parameters and their respective prior distributions are discussed next.

For parameters with little prior knowledge from the literature relatively objective prior distributions were chosen. The prior distributions in these cases were adjusted to allow wide range of parameters to be inferred in preliminary analyses on simulated data. Log-normal distributions were preferred for parameters with limited support due to physical reasoning.

2.2.1. Location parameter

The location parameter μ of GPD restricts the support of the distribution. GPD is conditional to observations $X > \mu$. When fitting GPD to PoT data and assuming the shape parameter $\xi < 0$, a mean excess plot is commonly utilized. A sufficiently large μ is to be chosen as the mean excess should become approximately linear after such threshold. [34, 7]

The prediction results have been reported to be relatively insensitive to the choice of the location parameter [7]. One might question why the critical defect size is not modeled using μ. The short answer is that the conditions for crack growth are potentially different for surface and internal cracks. The location parameter was here chosen to be $1\,\mu\mathrm{m}$, representing the size of a distinguishable inclusion.

2.2.2. Shape parameter

The shape parameter ξ is what dominates the high volume predictions of the model. The existence of an upper limit of inclusion size depends on the assumption that $\xi < 0$. The upper limit is strongly dependent on the shape parameter ξ, especially when ξ tends towards zero [32]. The shape parameter is crucial in determining the saturation rate of the characteristic inclusion size to the upper limit with an increase of prediction volume [32] –

more negative ξ results in more rapid saturation and vice versa. The aforementioned flexibility of modeling different kinds of observations of saturation comes with this parameter.

The prior distribution was chosen to be left truncated normal distribution

$$-\ln(-\xi) \sim \mathcal{N}(2.0, 0.7^2) \quad \text{conditional on } -1 < \xi < 0. \tag{12}$$

This choice allows practically everything between no saturation when ξ tends to zero and finite saturation when ξ is negative.

2.2.3. Scale parameter

The scale parameter σ also contributes to the upper limit of the inclusion size and variance of the inclusion size distribution. Its effect is emphasized in the smaller prediction volumes [32].

The maximum defect size $x_{\max}$ was chosen as a parameter as it had a clear lower bound (the maximum observed inclusion size) and its prior was chosen to be the log-normal distribution with the location parameter set to the largest observed inclusion:

$$\ln\left(x_{\max} - \max_i \sqrt{\text{area}_i}\right) \sim \mathcal{N}(4.0, 2.0^2). \tag{13}$$

For example, if $\max_i \sqrt{\text{area}_i}$ was 50 µm, then the 5% and 95% percentiles would be 52 µm and 1515 µm, respectively. The scale parameter σ was then calculated from (3).

2.2.4. Inclusion density

The inclusion density ρ [$1/\text{mm}^3$] is a measure of intensity of the Poisson point field. The number of inclusions found in volume V is a random variable that follows the Poisson distribution with the expected value of ρV. The inclusion density used here is conditional to the GPD location parameter $X > \mu$. Values between 1-100 are suggested in the literature [12, 8, 22].

The prior distribution for ρ was chosen to be log-normal with a rather high variance:

$$\ln \rho \sim \mathcal{N}(3.0, 4.7^2). \tag{14}$$

The 5% and 95% percentiles are 0.009 $1/\text{mm}^3$ and 45 744 $1/\text{mm}^3$, respectively.

2.2.5. Surface criticality factor

The surface defect can be rated to be generally more dangerous than the internal defect of similar size. By critical defect we mean the defect that reveals itself, i.e., wins the competition between different failure modes and is found from the fracture surface as the cause of fatigue failure. We thus define a surface criticality factor k that relates the surface and internal defect sizes to be as likely cause for the fatigue failure. The internal defect has to be k times bigger than the largest surface defect to be critical. Potential factors that affect the surface criticality factor are: fracture mechanical stress intensity factors [23], different crack growth rates, surface residual stresses and surface finishing quality. If the stress is not approximately homogeneous in the specimen's highly stressed volume (smooth specimen, axial loading), such surface criticality factor cannot be applied. In these cases, a spatial failure probability density function could be implemented and applied in the likelihood with more accurate details of the fatigue initiation location. This kind of approach additionally requires the fatigue relationship of stress level and defect size to be known or modeled.

Setting the surface and internal fatigue limits equal from [23] gives $k = (1.56/1.43)^6 \approx 1.69$. The prior distribution was chosen to be log-normal:

$$\ln k \sim \mathcal{N}(1.0, 1.0). \tag{15}$$

2.2.6. Other failure sources

When the most critical inclusion in the material is small enough, failures initiate from surface scratches, weak grains or the alike. In other words, there is an inherent flaw in the material that can be more critical than the largest non-metallic inclusion. The sizes of the other defects at the surface and subsurface are modeled as log-normally distributed random variables with their respective distribution parameters. The reason to distinguish between surface and subsurface with other failure sources is to be able to relate the respective defect sizes of the corresponding location's non-metallic inclusion sizes. We are thus able to use the surface criticality factor that should also affect the cracks initiated from other failure sources. This definition leads to the distributions being specific to the test geometry and manufacturing.

The priors for the hyperparameters of both surface and internal distributions were chosen to be

$$\mu_{\text{other}-j} \sim \mathcal{N}(2.0, 4.0^2), \quad j \in \{\text{int}, \text{surf}\} \tag{16}$$

$$\ln \sigma_{\text{other}-j} \sim \mathcal{N}(0.0, 1.0), \quad j \in \{\text{int}, \text{surf}\} \tag{17}$$

$$\ln x_{\text{other}-j} \sim \mathcal{N}(\mu_{\text{other}-j}, \sigma^2_{\text{other}-j}), \quad j \in \{\text{int}, \text{surf}\} \tag{18}$$

2.3. Fitting model

Likelihood-based fitting strategies are commonly utilized to fit the models, typically coupled with confidence intervals. Bayesian inference was used in [12]. For optical metallography of polished cross-sections, the Wicksell's corpuscle problem has to be utilized in order to find the true 3D-size distribution analytically [21, 40]. The fit for GPD from cross-section data is shown in [12], for Gumbel distribution in [9] and for log-normal distribution in [13]. A typical problem with the cross-section-based fit is the volume of samples needed to get statistically reliable estimates of the extremes (emphasized with the BM methods) [13] and the sensitivity of the fit becoming pronounced with an increase in the extrapolation volume. Larger volumes of metal can be studied with for example cold crucible remelting, electrolytic dissolution or electron beam button remelting [31]. A more reliable estimate of the inclusion density can be achieved based on these inclusion counting methods.

Another approach to fitting the models is calibrating the total failure probability at the stress levels close to the fatigue limit combined with the Kitagawa-Takahashi diagram [41, 42] or the Murakami model [23] providing the inclusion size-fatigue limit relationship [8, 16, 3, 36, 5, 4, 43, 19]. One problem with these kinds of fits is that, first of all, the failure probability is a result of statistical inference and prone to sample size errors; inferring the correct standard deviation of the fatigue limit from small samples is not an easy task. Another problem is that these fits typically neglect the observed failure initiation cause and can thus yield various defect distributions that do not necessarily represent the material's true defect distribution. Especially the inclusion density parameter remains difficult to calibrate to only fatigue test data and values of 1-100 defects/unit volume or area (in surface fatigue based models) are typically assumed [22, 8]. WL-based models that apply independent parameters to the area and volume failure probabilities are in danger of losing the connection of the defects originating from a joint statistical distribution. The relative explanatory power between defects and fatigue process can thus become unclear.

2.3.1. Likelihood

The likelihood function here accounts for the fracture surface observations. We identify four different failure initiation types:

- Surface non-metallic inclusion ($c = 0$), Figure 1a
- Internal non-metallic inclusion ($c = 1$), Figure 1b
- Surface other failure source (e.g. scratch or surface roughness) ($c = 2$), Figure 1c
- Internal other failure source (e.g. weak grain) ($c = 3$), Figure 1d

Examples of the different initiation types are shown in Figure 1. For the sake of simplicity, interaction of defects, clusters of inclusions and non-spherical shaped inclusions were neglected in this paper. Clusters and non-spherical shaped inclusions would alter the number of surface defects found on the surface, as the probability of an elongated inclusion penetrating the surface increases. The size distributions would also change, and we refer to [40] for Wicksell's corpuscle problem of the non-spherical shapes and [44] for the fatigue interpretation of these defects. The results of Abroug *et al.* [19] suggest that the fracture mechanical severity-index might not alone be enough to analyze the elongated inclusion shapes. A stochastic non-local approach, such as the WL, might be required to capture the increased probability of weak neighboring microstructure, as discussed in [45]. For micromechanics based fatigue analyses we refer to [46, 47].

The likelihood then depends on the observed failure mode, and it represents the fact that the namely location was critical and other locations were less critical. The likelihood that we use is

$$\mathcal{L}_i\left(\theta \mid x_i, c_i\right) = \begin{cases} f_{\text{surf}}\left(x_i \mid \theta\right) F_{\text{int}}\left(kx_i \mid \theta\right) F_{\text{other}-\text{surf}}\left(x_i \mid \theta\right) F_{\text{other}-\text{int}}\left(kx_i \mid \theta\right), & c_i = 0 \\ f_{\text{int}}\left(x_i \mid \theta\right) F_{\text{surf}}\left(x_i/k \mid \theta\right) F_{\text{other}-\text{surf}}\left(x_i/k \mid \theta\right) F_{\text{other}-\text{int}}\left(x_i \mid \theta\right), & c_i = 1 \\ \int f_{\text{other}-\text{surf}}\left(x \mid \theta\right) F_{\text{int}}\left(kx \mid \theta\right) F_{\text{surf}}\left(x \mid \theta\right) F_{\text{other}-\text{int}}\left(kx \mid \theta\right) \mathrm{d}x, & c_i = 2 \\ \int f_{\text{other}-\text{int}}\left(x \mid \theta\right) F_{\text{int}}\left(x \mid \theta\right) F_{\text{surf}}\left(x/k \mid \theta\right) F_{\text{other}-\text{surf}}\left(x/k \mid \theta\right) \mathrm{d}x, & c_i = 3 \end{cases} \tag{19}$$

where x_i is the observed inclusion size at the fracture surface and θ represents the parameter vector. The total likelihood is obtained by taking the product of the likelihoods of all observations. In case of more failure sources were recognized and included in the analysis, e.g. another non-metallic inclusion distribution, the likelihoods would be multiplied with the additional distribution functions. For the non-inclusion initiated failures the size is thought to be unobserved, and thus the integrals represent the probability of failure from non-inclusion. This convention is seen necessary as determining the comparable sizes of scratches or grain initiated failures to non-metallic inclusions is a difficult task from the fracture surfaces and could induce subjective bias between different operators. The critical inclusion has an original size distribution that is different from the underlying extreme value distribution because it is conditional on the fact that the other failure modes were less critical. This distribution depends on the specimen geometry. To our best knowledge, this has not been presented anywhere else.

The essence of this paper is in this likelihood; we utilize all the information available from the observation – even including what was not observed! By this way, we find the parameters of the non-metallic inclusion distribution that is compliant with the observed inclusion sizes and gives a realistic probability of failure to each failure mode with respect to the observations. With the surface and internal having different inspection volumes, we simultaneously fit the volume sensitivity of the model. The non-inclusion initiated failures on the other hand help fit the inclusion density parameter ρ. These are seen as clear benefits over other approaches fitting the defect distribution models to fatigue tests. Even with a data set containing only surface failures, it is useful to check that the probability of internal failure is in agreement with the observations.

2.3.2. Posterior distribution

The parameter posterior distribution is obtained by the Bayes rule

$$p(\theta \mid \bar{y}) = \frac{p(\bar{y} \mid \theta)p(\theta)}{p(\bar{y})}, \tag{20}$$

where $\bar{y}$ denotes the data vector containing (x_i, c_i) pairs, $p(\bar{y} \mid \theta)$ is the total likelihood function constructed from (19), $p(\theta)$ is the prior constructed from product of each probability distribution function described in the priors in section 2.2, and $p(\bar{y}) = \int p(\bar{y} \mid \theta)p(\theta)d\theta$ is the marginal probability. The posterior distribution was solved numerically using Markov Chain Monte Carlo (MCMC) method. More details of the numerical solution are given in the beginning of section 4.

2.4. Limitations of the model

The assumptions of the model are

- Inclusions are approximately spherical
- Inclusions are approximately uniformly distributed in the volume
- GPD can describe the inclusion size distribution
- An upper limit for inclusion size exists when volume tends to infinity ($\xi < 0$)
- Direct interaction of distinguished failure sources is neglected, e.g. a non-metallic inclusion at the bottom of a machining scratch or clusters of inclusions
- In smooth axial fatigue specimen, the criticality difference between surface and internal defects can be described by a load-level independent factor
- All failure types can compete, and only the most critical is observed
- Runout level (history) does not affect the outcome of retesting

The model predictions can thus be questioned for heavily formed materials with clusters of inclusions, high aspect ratio inclusions and grainflow. Less error is caused if the loading direction is parallel to the grainflow. The load-level independence of the model causes probably more error if tests are performed on very different load levels or the material exhibits signs of surface fatigue limit (discontinuous SN-curve). The errors from these sources can be alleviated if load levels and conditions have been relatively similar (for example high-cycle fatigue), a continuously decreasing SN-curve is observed, and surface failures are observed from very small inclusions. The history independence can be tolerated in situations where the runout load levels have been significantly lower than the retest/failure load levels, signs of very high cycle fatigue (optically dark area/fine-grained area) have not been observed at the fracture surfaces or the material is not subject of significant coaxing effect. Further condition for history independence is no significant pre-damaging at the previous test levels, so that statistical selection [48] alone explains majority of the behavior.

The lack of fatigue life in the analysis model requires more caution in the use of the current model. Stochastic analysis of low cycle fatigue and material variability has been studied in [49]. Murakami and Miller experimentally showed the effect of defect size to the fatigue life [50].

Removing these limitations is subject to future development work of the model. On the more optimistic side, the Bayesian framework offers excellent user-model-user communication if the model does not correctly represent the observations. For example, such problems may be exposed by comparing predictions of the model to the observations [51].

3. Experimental

Series of high-cycle fatigue tests were conducted using axial ultrasonic fatigue testing device to test the model. The material was quenched and tempered X40CrSiMo10-2 martensitic steel. The chemical composition is shown in Table 1. The mechanical properties of the material are given in Table 2.

C	Si	Mn	P	S	Ni	Cr	Mo	Cu
0.39	1.84	0.31	0.028	0.004	0.15	10.04	0.72	0.06

Table 1: Chemical composition of the material in weight %.

Yield strength [MPa]	Tensile strength [MPa]	Hardness [HBW]	Elongation [%]
731	974	286	19

Table 2: Mechanical properties of the material.

The specimen was a smooth specimen with 3.6 mm diameter, 5 mm long straight gauge section and 15 mm radius fillets at the shoulders of the specimen. The specimens were carefully mechanically polished, and the resulting diameter was on average 3.5 mm. Tests were performed in three temperatures: 300 °C, 400 °C and 600 °C and two stress ratios were used: $R = -1$ and $R = 0$. The runout limit was chosen to be 10^8 cycles. For each runout specimen, the load level was increased until fatigue failure was observed and finally the fracture surfaces of each specimen were inspected with a scanning electron microscope (SEM). The inclusion size measured from the fracture surface is assumed to sufficiently represent the real/effective size of the inclusion. A total of 80 specimens were tested and inspected. The fatigue crack initiation and growth was observed from the drop of the resonance frequency of the specimen. Once crack initiation was observed, the test was interrupted. A static tensile loading was applied and the specimen fatigued to failure with positive stress ratio to avoid ruining the fracture surfaces. The different types of fracture initiations found from the fracture surfaces are shown in Figure 1.

The fatigue failure sources were divided into spherical inclusions and other failure sources. The division was based on the fact that majority of the non-metallic impurities at the fatigue fracture initiation location were spherical inclusions: 1) calcium aluminates (CaO-Al_2O_3), 2) Al_2O_3-xMgO spinels embedded in calcium aluminates and 3) aluminium oxides A_2O_3. Most of these inclusion types were encapsulated with a calcium sulphide (CaS) shell. The rest of the inclusions were titanium nitrides (2 pcs) and spherical Al_2O_3-MnO spinel type inclusion (1 pc.). The TiN inclusions found at fracture surfaces were some of the smallest inclusions that is in line with the findings reported in [24, 13]. In addition, three SiC containing surface defects were found from the fracture initiation location. These types of particles were not found from the internal inclusion failures and therefore it may be concluded that the SiC particles embedded in the specimen surface are most likely residues from the mechanical polishing process. Only the spherical aluminates and oxides were chosen to be described with the GPD. Other inclusions, namely the TiN and SiC, were moved to the other-category of failure sources. Eventually, 56 spherical inclusions were taken into account in the GPD. The other-category comprised altogether of 24 incidents, of which 5 were non-metallic inclusions. The amounts of failures from each failure initiation types are shown in Table 3.

	Inclusion		Other failure source		
	Surface	Internal	Surface	Internal	$\sum$
Amount	10	46	16	8	80

Table 3: Amount of observations from each failure initiation type.

No discontinuous SN-curve was observed for the material. At the lower temperatures, signs of the transition from surface to internal failures was observed as a function of loading cycles. At the highest temperature, no systematic transition was observed. The failures occurred at somewhat similar loading levels: the relative standard deviation of the failure load was 8% in 300 °C, R=-1 tests. The observed sizes of fatigue failures initiating from non-metallic inclusions are shown in Figure 4.

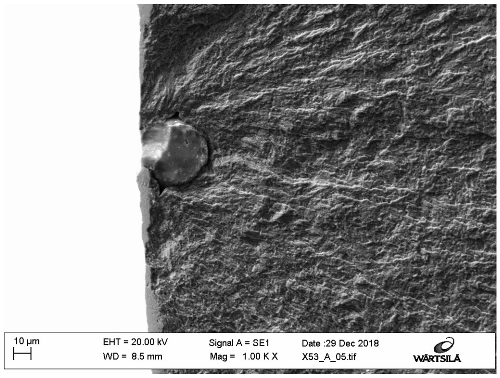

(a) Surface inclusion.

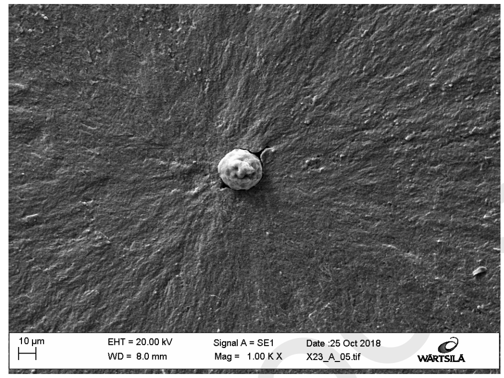

(b) Internal inclusion.

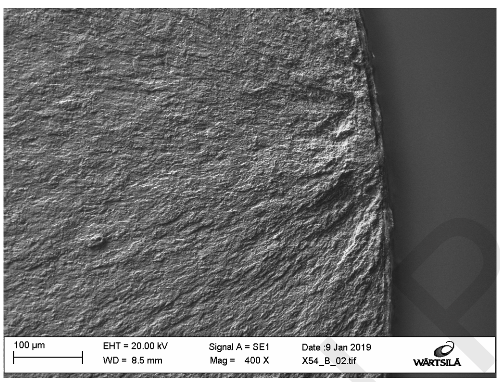

(c) Surface other failure source.

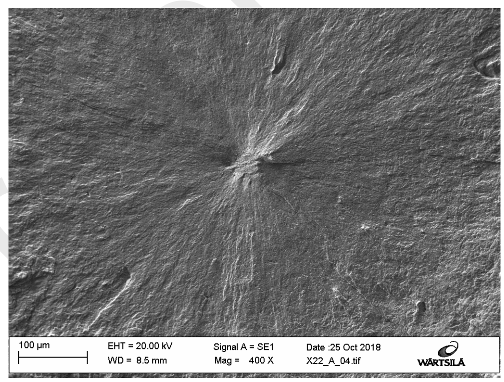

(d) Internal other failure source.

Figure 1: The different types of failure initiation types in X40CrSiMo10-2.

4. Results

The model was built and fitted to the experimental fracture surface observations using Markov Chain Monte Carlo (MCMC) method in statistical computation platform Stan [52, 53] version 2.18.0 using the No-U-Turn Sampler (NUTS). The statistical inference model and prior distributions were first calibrated to be able to robustly infer the model parameters from simulated data with various parameters before we proceeded to the real data. Numerical integration procedure was applied in the computation of the likelihood. Four independent Markov chains were used in the final inference, each with 10000 samples of which the first 5000 were used for warm-up of the sampler and excluded from the analysis. The Stan convergence indicators

[51] were good already with 2000 samples per chain indicating no problems with the inference, but higher resolution of the parameters is achieved with a greater number of samples. The result is a trace of parameter samples from the posterior distribution visualized in Figure 2. An interesting point to be made of the parameters is that the expected value of the inclusion density ρ is 0.23 $[1/\mathrm{mm}^3]$ which is very low compared to what others have proposed for other materials. Also, the surface criticality factor seems to be getting rather high values – the expected value is 5.75, and the one percent quantile is 2.35. Compared to the prior distribution the inference only ruled out the possibility of the surface criticality factor being too low.

The predictive probabilities of failure from each location and the observed failure probabilities are shown in Figure 3. The most significant discrepancy is in the surface failure probability that, by comparing the expected value to the observed, seems to be underestimated by roughly 5%. On the other hand, the probability of internal failure is over-estimated by a similar amount. In conjunction with the earlier observation that the inclusion density was surprisingly low, we checked whether the mere occurrence of surface inclusion caused the surface failures. Indeed, given at least one inclusion at the surface, the probability of failure from surface inclusion was 61% in our predictions. The probability of failure from internal inclusion in such case was approximately 23%, surface other sources 11% and internal other sources 5%.

Predictions were made from the posterior trace so that Poisson distributed defects were simulated to 20 fatigue specimen from each set of parameters (total of 400000 simulated specimen), and the size and the location of the most critical defect were captured. The predictive distributions for the critical surface and internal inclusions are shown with the observed sizes in Figure 4. The predictive distributions of the largest inclusions in respective locations are also shown. The density functions are normalized with the predicted probability of failure from the respective locations. It can be seen that the predicted failure sizes are in good agreement with the observed sizes and the maximum and critical sizes follow their respective distributions. The discrepancy between critical and maximum distributions is ought to increase when there is no single dominant failure type.

In Figure 5 the volume extrapolation capabilities of the fit model are highlighted. The shown quantiles are for the largest internal inclusion. The model prediction credibility regions (CR) are plotted for the critical inclusions as well. The horizontal histograms show the predictive distributions of the other failure sources' representative sizes. The different effective volumes

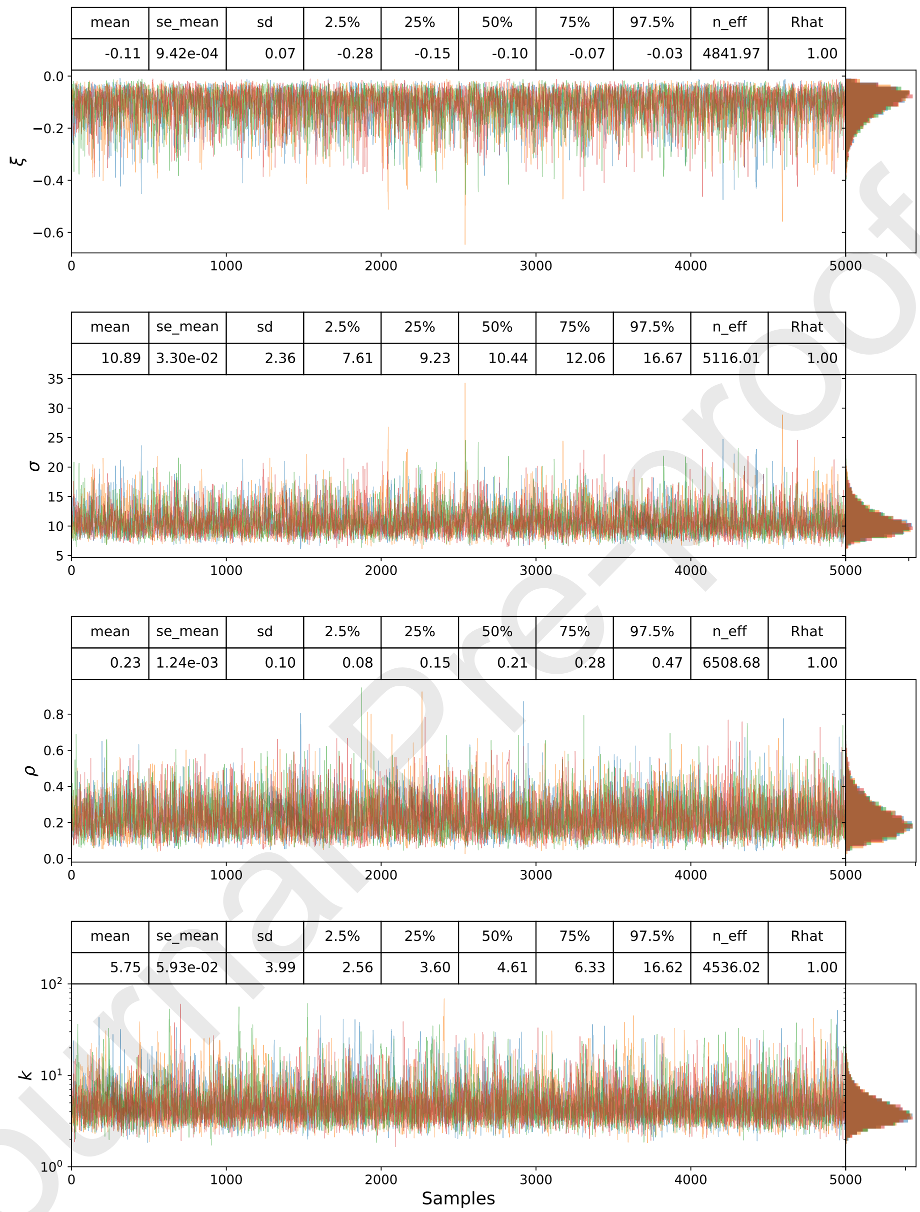

Figure 2: Posterior parameter traces of ξ, σ, ρ and surface criticality factor k. Different colors represent different chains. Convergence indicators, representative statistics and quantiles at the top of each parameter trace in tabular form.

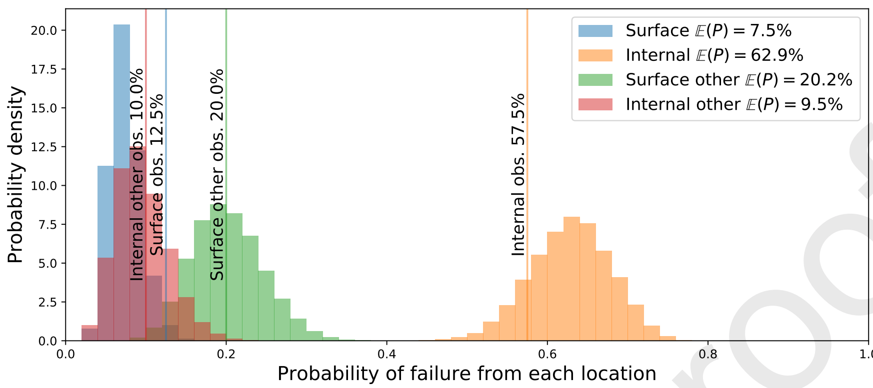

Figure 3: Predicted probabilities of failure from each location.

for surface and internal inclusions can also be seen from this Figure.

5. Discussion

A method for inferring non-metallic inclusion data from axial smooth fatigue specimens' fracture surfaces has been presented. It has been shown that in the case of a competition of two or more failure sources with different fatigue severity the sizes of the most critical inclusions follow a modified distribution from the block maxima distribution. Taking the different failure modes into account constraints the underlying inclusion size distribution and further aids the fit to be more compliant with the observations and more credible volume extrapolations can thus be made. The model was fit to the experimental fracture surface data, and the prediction distributions were in good agreement with the observations. The current model is load-level independent, meaning that the model might lack important explanatory mechanisms, such as the surface fatigue limit. The model utilized low inclusion density values and high surface criticality factors to explain the surface inclusion initiated failure observations. The low inclusion density is also supported by the observed amount of non-inclusion initiated failures. With the introduction of the surface fatigue limit to the model, it is expected that the likelihood of observing small internal inclusions increases at lower load levels and the critical surface inclusion size distribution is weighted to larger sizes.

Had the inclusions been measured also using the direct methods, such as optical microscopy from polished cross-sections, the fit of the model could

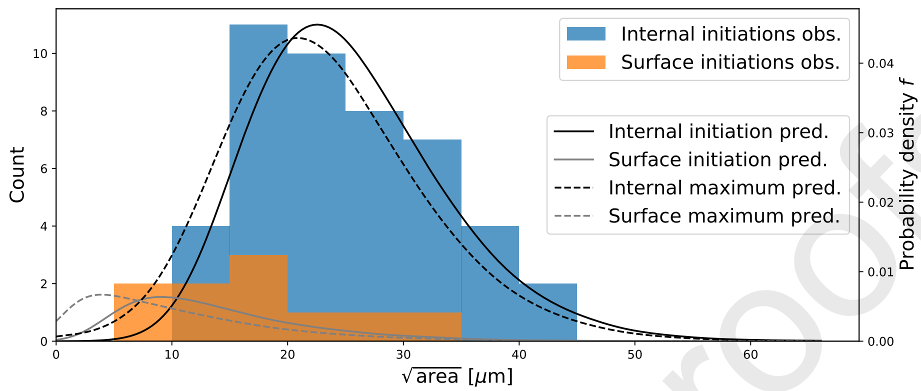

Figure 4: Prediction distributions and observed critical defect sizes from surface and internal inclusions and the maximum distributions.

be verified at least quantitatively. If the result of such measurement showed the fit parameters to be erroneous, it would serve as further motivation for improving the description of the fatigue process in the model – considering the rigorous statistical framework developed for the analysis of inclusions. In the current version of the model, the analysis of fatigue effects was on purpose kept light: a surface criticality factor was used to describe multiple effects leading to surface defects being more critical than internal defects of the same size. (Although the possibility of it being the other way around was not ruled out in the prior distribution for the parameter). This kind of description can only be applied to homogeneous stress fields where categorization of only surface and internal failure locations to be different in terms of fatigue is possible. With such systematic approach to developing the model with minimal fatigue assumptions, the relative explanatory power between fatigue and statistically distributed defects is not compromised. With typical notched specimen or bending/torsion loading, the crack is promoted to initiate in specific locations effectively nullifying the competition. In this light, the potential value of axial smooth fatigue tests is increased compared to the other test methods. The failures initiated from different inclusion types than the aluminates and oxides should be analyzed using separate size distributions to account for the competition of different failure modes properly. Modeling TiN with its own size distribution in the inference would, however, double the number of parameters in the inference and introduce questions regarding the relative severity of each inclusion decomposition, and was thus

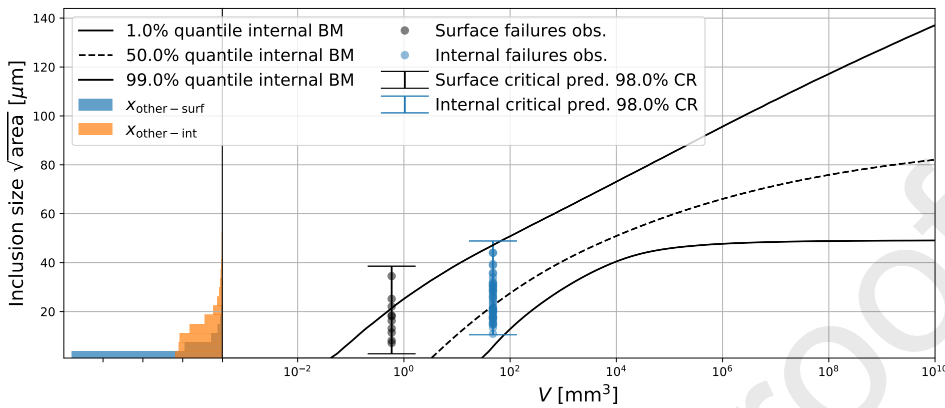

Figure 5: Predicted volume extrapolation effect. The prediction quantiles are for the largest internal inclusion. The credibility regions are for the model predictions of critical inclusions shown in Figure 4.

left out of the current paper. As long as the log-normal distribution sufficiently represents the specimen-specific distributions for the other failure sources' equivalent defect sizes, this is not a problem.

The better quantification of non-metallic inclusions can be used to design safer machine components, support the dynamic risk assessment of fatigue failure in analysis of complex systems [54, 55], identify problems in the manufacturing processes, comparison of suppliers and defining the normal for quality control purposes.

5.1. Conclusions

The goal of this paper was to further develop the statistical methodology for fitting the inclusion size distributions and predicting the critical sizes. The findings are summarized below:

- The inclusion size distribution obtained with fatigue testing is conditional on the other failure sources and thus different than the block maxima distribution.
- The presented methodology takes the above into consideration while fitting the size distribution yielding new constraints to the parameters.
- Observation of the most critical inclusion simultaneously limits the possible largest sizes of other failure sources, further enhancing the volume extrapolation capabilities of the model.

- The predictions given by the presented method are compatible with the experiments.
- Axial smooth fatigue tests with fractography yield great information potential of the underlying inclusion distributions.
- Inclusion types should be categorized and modeled with separate size distributions to account for the competition of failure types properly.

6. Acknowledgements

This study was conducted as part of the WIMMA (Dnro 1566/31/2015) -research project. The authors are grateful for the financial support provided by Business Finland Oy (former Tekes) and Wärtsilä Finland Oy.

References

[1] W. Weibull, A statistical theory of strength of materials, IVB-Handl.

[2] J. Böhm, K. Heckel, Die vorhersage der dauerschwingfestigkeit unter berücksichtigung des statistischen größeneinflusses, Materialwissenschaft und Werkstofftechnik 13 (4) (1982) 120–128. doi:10.1002/mawe.19820130408.

[3] A. Wormsen, B. Sjödin, G. Härkegård, A. Fjeldstad, Non-local stress approach for fatigue assessment based on weakest-link theory and statistics of extremes, Fatigue & Fracture of Engineering Materials & Structures 30 (12) (2007) 1214–1227. doi:10.1111/j.1460-2695.2007.01190.x.

[4] H. Bomas, T. Linkewitz, P. Mayr, Application of a weakest-link concept to the fatigue limit of the bearing steel sae 52100 in a bainitic condition, Fatigue & Fracture of Engineering Materials & Structures 22 (9) (1999) 733–741. doi:10.1046/j.1460-2695.1999.t01-1-00211.x.

[5] S. Sadek, M. Olsson, The probability of hcf–surface and sub-surface models, International Journal of Fatigue 92 (2016) 147–158. doi:10.1016/j.ijfatigue.2016.06.021.

[6] Y. Murakami, H. Usuki, Quantitative evaluation of effects of non-metallic inclusions on fatigue strength of high strength steels. ii: Fatigue limit evaluation based on statistics for extreme values of inclusion size, International Journal of Fatigue 11 (5) (1989) 299–307. doi:10.1016/0142-1123(89)90055-8.

[7] G. Shi, H. Atkinson, C. Sellars, C. Anderson, Application of the generalized pareto distribution to the estimation of the size of the maximum inclusion in clean steels, Acta Materialia 47 (5) (1999) 1455–1468. doi:10.1016/S1359-6454(99)00034-8.

[8] M. Makkonen, Statistical size effect in the fatigue limit of steel, International Journal of Fatigue 23 (5) (2001) 395–402. doi:10.1016/S0142-1123(01)00003-2.

[9] A. Cetin, A. Naess, Statistical characterisation of inclusions in metals: from 2d to 3d, Materials Science and Technology 28 (8) (2012) 965–970. doi:10.1179/1743284712Y.0000000038.

[10] A. Cetin, A. Naess, G. Härkegård, A physically based extreme value characterization of material fatigue, International Journal of Fatigue 47 (2013) 216–221. doi:10.1016/j.ijfatigue.2012.09.003.

[11] Y. Murakami, T. Toriyama, E. Coudert, Instructions for a new method of inclusion rating and correlations with the fatigue limit, Journal of Testing and Evaluation 22 (4) (1994) 318–326. doi:10.1520/JTE11840J.

[12] C. W. Anderson, S. Coles, The largest inclusions in a piece of steel, Extremes 5 (3) (2002) 237–252. doi:10.1023/A:1024025027522.

[13] A. Cetin, A. Roiko, M. Lind, Towards proper sampling and statistical modelling of defects, Fatigue & Fracture of Engineering Materials & Structures 38 (9) (2015) 1056–1065. doi:10.1111/ffe.12317.

[14] J. Böhm, Zur vorhersage von dauerschwingfestigkeiten ungekerbter und gekerbter bauteile unter berücksichtigung des statistichen grösseneinflusses, Ph.D. thesis, Technische Universität München (1980).

[15] W. Magin, Untersuchung des geometrischen Grösseneinflusses bei Umlaufbiegebeanspruchung unter besonderer Berücksichtigung technologischer Einflüsse: Dissertation, Technische Hochschule, 1981.

[16] L. Flaceliere, F. Morel, Probabilistic approach in high-cycle multiaxial fatigue: volume and surface effects, Fatigue & Fracture of Engineering Materials & Structures 27 (12) (2004) 1123–1135. doi:10.1111/j.1460-2695.2004.00823.x.

[17] K. Karlén, M. Olsson, Experimental and statistical investigation of the weakest link integral and the volume effect, Procedia Engineering 2 (1) (2010) 1451–1457. doi:10.1016/j.proeng.2010.03.157.

[18] K. Karlén, M. Olsson, A study of the volume effect and scatter at the fatigue limit–experiments and computations for a new specimen with separated notches, International Journal of Fatigue 33 (3) (2011) 363–371. doi:10.1016/j.ijfatigue.2010.09.012.

[19] F. Abroug, E. Pessard, G. Germain, F. Morel, Hcf of aa7050 alloy containing surface defects: Study of the statistical size effect, International Journal of Fatigue 110 (2018) 81–94. doi:10.1016/j.ijfatigue.2018.01.012.

[20] F. Abroug, E. Pessard, G. Germain, F. Morel, A probabilistic approach to study the effect of machined surface states on hcf behavior of a aa7050 alloy, International Journal of Fatigue 116 (2018) 473–489. doi:10.1016/j.ijfatigue.2018.06.048.

[21] S. Wicksell, The corpuscle problem: a mathematical study of a biometric problem, Biometrika (1925) 84–99doi:10.2307/2332027.

[22] A. Cetin, G. Härkegård, A. Naess, The fatigue limit: An analytical solution to a monte carlo problem, International Journal of fatigue 55 (2013) 194–201. doi:10.1016/j.ijfatigue.2013.06.015.

[23] Y. Murakami, M. Endo, Effects of defects, inclusions and inhomogeneities on fatigue strength, International Journal of Fatigue 16 (3) (1994) 163–182. doi:10.1016/0142-1123(94)90001-9.

[24] A. Melander, P. Ölund, Detrimental effect of nitride and aluminium oxide inclusions on fatigue life in rotating bending of bearing steels,

Materials Science and Technology 15 (5) (1999) 555–562. doi:10.1179/026708399101506094.

[25] D. Spriestersbach, P. Grad, E. Kerscher, Influence of different non-metallic inclusion types on the crack initiation in high-strength steels in the vhcf regime, International Journal of Fatigue 64 (2014) 114–120. doi:10.1016/j.ijfatigue.2014.03.003.

[26] D. Spriestersbach, P. Grad, E. Kerscher, Crack initiation mechanisms and threshold values of very high cycle fatigue failure of high strength steels, Procedia Engineering 74 (2014) 84–91. doi:10.1016/j.proeng.2014.06.229.

[27] U. Karr, R. Schuller, M. Fitzka, B. Schönbauer, D. Tran, B. Pennings, H. Mayer, Influence of inclusion type on the very high cycle fatigue properties of 18ni maraging steel, Journal of Materials Science 52 (10) (2017) 5954–5967. doi:10.1007/s10853-017-0831-1.

[28] S. Beretta, C. Anderson, Y. Murakami, Extreme value models for the assessment of steels containing multiple types of inclusion, Acta Materialia 54 (8) (2006) 2277–2289. doi:10.1016/j.actamat.2006.01.016.

[29] Y. Murakami, S. Beretta, Small defects and inhomogeneities in fatigue strength: experiments, models and statistical implications, Extremes 2 (2) (1999) 123–147. doi:10.1023/A:1009976418553.

[30] C. Anderson, G. Shi, H. Atkinson, C. Sellars, J. Yates, Interrelationship between statistical methods for estimating the size of the maximum inclusion in clean steels, Acta Materialia 51 (8) (2003) 2331–2343. doi:10.1016/S1359-6454(03)00041-7.

[31] H. Atkinson, G. Shi, Characterization of inclusions in clean steels: a review including the statistics of extremes methods, Progress in Materials Science 48 (5) (2003) 457–520. doi:10.1016/S0079-6425(02)00014-2.

[32] G. Shi, H. Atkinson, C. Sellars, C. Anderson, J. Yates, Computer simulation of the estimation of the maximum inclusion size in clean steels by the generalized pareto distribution method, Acta Materialia 49 (10) (2001) 1813–1820. doi:10.1016/S1359-6454(01)00079-9.

[33] J. Yates, G. Shi, H. Atkinson, C. Sellars, C. Anderson, Fatigue tolerant design of steel components based on the size of large inclusions, Fatigue & Fracture of Engineering Materials & Structures 25 (7) (2002) 667–676. doi:10.1046/j.1460-2695.2002.00523.x.

[34] S. Coles, J. Bawa, L. Trenner, P. Dorazio, An introduction to statistical modeling of extreme values, Vol. 208, Springer, 2001. doi:10.1007/978-1-4471-3675-0.

[35] H. Kaufmann, D. Wolters, Zyklische beanspruchbarkeit dickwandiger bauteile aus ferritischem gußeisen mit kugelgraphit, Konstruieren und Giessen 27 (1) (2002) 4–27.

[36] G. Härkegård, G. Halleraker, Assessment of methods for prediction of notch and size effects at the fatigue limit based on test data by böhm and magin, International Journal of Fatigue 32 (10) (2010) 1701–1709. doi:10.1016/j.ijfatigue.2010.03.011.

[37] Y. Murakami, Inclusion rating by statistics of extreme values and its application to fatigue strength prediction and quality control of materials, Journal of Research of the National Institute of Standards and Technology 99 (1994) 345–345.

[38] M. Väntänen, J. Vaara, J. Aho, J. Kemppainen, T. Frondelius, Bayesian sequential experimental design for fatigue tests, Rakenteiden Mekaniikka 50 (3) (2017) 201–205. doi:10.23998/rm.64924.

[39] X. Liu, D. Lu, P. Hoogenboom, Hierarchical bayesian fatigue data analysis, International Journal of Fatigue 100 (2017) 418–428. doi:10.1016/j.ijfatigue.2017.03.043.

[40] S. Wicksell, The corpuscle problem: second memoir: case of ellipsoidal corpuscles, Biometrika (1926) 151–172doi:10.2307/2332500.

[41] H. Kitagawa, S. Takahashi, Applicability of fracture mechanics to very small cracks or the cracks in the early stage, Proc. of 2nd ICM, Cleveland, 1976 (1976) 627–631.

[42] M. El Haddad, T. Topper, K. Smith, Prediction of non propagating cracks, Engineering Fracture Mechanics 11 (3) (1979) 573–584. doi:10.1016/0013-7944(79)90081-X.

[43] D. Sandberg, R. Mansour, M. Olsson, Fatigue probability assessment including aleatory and epistemic uncertainty with application to gas turbine compressor blades, International Journal of Fatigue 95 (2017) 132–142. doi:10.1016/j.ijfatigue.2016.10.001.

[44] Y. Murakami, M. Endo, Quantitative evaluation of fatigue strength of metals containing various small defects or cracks, Engineering Fracture Mechanics 17 (1) (1983) 1–15. doi:10.1016/0013-7944(83)90018-8.

[45] J. Vaara, A. Mäntylä, T. Frondelius, Brief review on high-cycle fatigue with focus on non-metallic inclusions and forming, Rakenteiden Mekaniikka 50 (3) (2017) 146–152. doi:10.23998/rm.65048.

[46] M. D. Sangid, The physics of fatigue crack initiation, International journal of fatigue 57 (2013) 58–72. doi:10.1016/j.ijfatigue.2012.10.009.

[47] A. Laukkanen, M. Lindroos, T. Andersson, T. Verho, T. Pinomaa, Micromechanical modeling of failure behavior of metallic materials, Rakenteiden Mekaniikka 50 (3) (2017) 271–274. doi:10.23998/rm.65161.

[48] H.-P. Gänser, J. Maierhofer, T. Christiner, Statistical correction for reinserted runouts in fatigue testing, International Journal of Fatigue 80 (2015) 76–80. doi:10.1016/j.ijfatigue.2015.05.015.

[49] S. Zhu, S. Foletti, S. Beretta, Probabilistic framework for multiaxial lcf assessment under material variability, International Journal of Fatigue 103 (2017) 371–385. doi:10.1016/j.ijfatigue.2017.06.019.

[50] Y. Murakami, K. Miller, What is fatigue damage? a view point from the observation of low cycle fatigue process, International Journal of Fatigue 27 (8) (2005) 991–1005. doi:10.1016/j.ijfatigue.2004.10.009.

[51] A. Gelman, H. Stern, J. Carlin, D. Dunson, A. Vehtari, D. Rubin, Bayesian data analysis, Chapman and Hall/CRC, 2013. doi:10.1201/b16018.

[52] B. Carpenter, A. Gelman, M. Hoffman, D. Lee, B. Goodrich, M. Betancourt, M. Brubaker, J. Guo, P. Li, A. Riddell, Stan: A probabilistic programming language, Journal of Statistical Software 76 (1). doi:10.18637/jss.v076.i01.

[53] Stan Development Team, PyStan: the Python interface to Stan, version 2.17.1.0 (2017).
URL http://mc-stan.org/

[54] N. Khakzad, F. Khan, P. Amyotte, Dynamic risk analysis using bow-tie approach, Reliability Engineering & System Safety 104 (2012) 36–44. doi:10.1016/j.ress.2012.04.003.

[55] N. Khakzad, F. Khan, P. Amyotte, V. Cozzani, Domino effect analysis using bayesian networks, Risk Analysis: An International Journal 33 (2) (2013) 292–306. doi:10.1111/j.1539-6924.2012.01854.x.

- The inclusion size distribution from fatigue testing is filtered by fatigue process
- Observation of an inclusion limits the possible sizes of other failure sources
- The presented model has enhanced fatigue size effect prediction capabilities